Does DrugCLIP Find the Right Pocket? A Systematic Evaluation of Binding-Site Identification Across 42 Drug Targets

Bocheng Xie , Xiaokang Guo , Pengwei Xiao * , Chao Yang *

Posted Date: 2 April 2026

doi: 10.20944/preprints202604.0204.v1

Keywords: binding pocket identification; contrastive learning; benchmarking dataset; traditional pocket detection workflow; structure-based virtual screening

 doi:10.20944/preprints202604.0204.v1

Article

Does DrugCLIP Find the Right Pocket? A Systematic Evaluation of Binding-Site Identification Across 42 Drug Targets

Bocheng Xie [1], Xiaokang Guo [2], Pengwei Xiao [1,*] and Chao Yang [1,*]

[1] Faculty of Pharmaceutical Sciences, Shenzhen University of Advanced Technology, Shenzhen 518107, China
[2] Institute of Intelligent Innovation, Henan Academy of Sciences, Zhengzhou 451162, China
* Correspondence: yang.chao@suat-sz.edu.cn (C.Y.); xiaopengwei@suat-sz.edu.cn (X.G.)

Abstract

Contrastive learning–based models such as DrugCLIP have recently emerged as scalable tools for structure-based virtual screening by embedding protein structures and small molecules into a shared representation space. While these approaches demonstrate high throughput and competitive screening performance in ligand retrieval tasks, their ability to correctly identify biologically relevant ligand-binding pockets has not been systematically evaluated. Here, we construct a benchmarking dataset comprising 42 pharmacologically diverse human protein targets with experimentally validated drug-bound structures spanning multiple target families. Using this dataset, we evaluate the pocket recognition capability of DrugCLIP and compare its performance with a traditional structure-based workflow that integrates geometric pocket detection (Fpocket) with dynamics-informed pocket ranking (ESSA). DrugCLIP achieves perfect success rates for several well-studied target classes, including kinases (10/10), GPCRs (5/5), and nuclear receptors (5/5), but shows markedly reduced performance for ion channels (1/4) and transporters (2/5). Notably, pocket prediction accuracy does not strongly correlate with structural data availability, suggesting that intrinsic pocket characteristics rather than training data abundance primarily affect model performance. Across the benchmark, DrugCLIP does not outperform traditional pocket identification strategies (DrugCLIP vs. Fpocket+ESSA: 74% vs. 79%). Together, these results provide a quantitative evaluation of pocket recognition by contrastive learning–based models and highlight key limitations that should be considered when applying embedding-based approaches in prospective structure-based drug discovery.

Keywords: binding pocket identification; contrastive learning; benchmarking dataset; traditional pocket detection workflow; structure-based virtual screening

1. Introduction

Structure-based drug discovery (SBDD) relies fundamentally on the accurate identification of ligand-binding pockets, which define the structural context for molecular recognition and determine the reliability of downstream docking, scoring, and lead optimization [1–6]. Typically, the binding pocket used for docking is already known from prior structural information. For example, the binding site is chosen based on the information of co-crystallized ligand/substrate binding site, such as ATP binding site or protein-protein interactions (PPI) interface. However, when the binding site information is missing or when a novel binding pocket needs to be explored, identifying the relevant ligandable pocket becomes a critical starting point. Traditionally, two major computational strategies have been extensively used to address this challenge: blind docking and pocket detection algorithms. Blind docking attempts to search the entire protein surface for energetically favorable ligand-binding

 doi:10.20944/preprints202604.0204.v1

modes [7,8], but this approach is often computationally demanding because of the large spatial search space. Alternatively, pocket detection methods aim to effectively identify plausible ligand-binding cavities directly from protein structures. Several widely used software, including Fpocket [9], FTMap [10], SiteMap [11], MDpocket [12] and AlphaSpace [13,14], identify pockets by analyzing surface cavities, geometric features, residue environment, or favorable interaction hot spots defined by chemical probes. The resulting candidate pockets are then ranked, and top-ranking pockets are used to guide subsequent docking or experimental validation.

The rapid growth of structural biology and artificial intelligence has significantly expanded the landscape of SBDD [15]. In particular, deep learning methods for protein structure prediction, including AlphaFold2 [16] and RoseTTAFold [17], have greatly increased access to high-quality three-dimensional protein models. These advances have broadened the scope of SBDD by making structural models available at unprecedented scale. At the same time, this expansion has created new demand for deep learning methods that can efficiently identify and prioritize biologically active compounds from vast chemical spaces. Recently, deep learning approaches for protein-ligand modelling have begun to move beyond traditional physics-based docking [18–21]. For example, contrastive learning-based models [22–24] such as DrugCLIP [22] embed protein structures and small molecules into a shared latent space, enabling rapid ligand retrieval across large chemical libraries.

These contrastive learning-based methods offer substantial gains in high throughput and have demonstrated competitive performance in retrospective virtual screening benchmarks, suggesting that learned embeddings can capture relevant aspects of protein-ligand compatibility. However, strong performance in ligand ranking does not necessarily imply accurate representation of ligand binding pocket [25]. In practical SBDD, correct localization of the functional ligand-binding site is a prerequisite for reliable downstream modelling [26]. A model may retrieve chemically compatible ligands yet still fail to prioritize the true pharmacologically relevant pocket. Thus, the ability of contrastive learning-based models to identify the correct binding site should be evaluated independently rather than assumed from retrospective virtual screening performance. Most existing benchmarks [22,27] focus on ligand retrieval, enrichment, or binding affinity prediction, implicitly assuming that meaningful pocket identification is already achieved as part of the learning process. This assumption may hold for proteins with well-defined conserved cavities, such as kinases or nuclear receptors, but it may break down for more challenging systems. Therefore, a rigorous evaluation of pocket recognition ability is necessary to access the practical strengths and limitations of these methods in read-world drug discovery campaigns.

To address this gap, we constructed a benchmarking dataset of 42 pharmacologically relevant and structurally diverse human protein targets spanning seven major target families (Figure 1), each represented by an experimentally determined drug-bound structure. Using this dataset, we systematically evaluated the ability of DrugCLIP to identify the correct ligand-binding pocket and compared its performance with a conventional structure-based workflow combining geometric pocket detection (Fpocket) [9] and dynamics-informed pocket ranking (ESSA) [28]. By examining performance across protein classes with distinct structural and functional characteristics, our results provide a direct assessment of the pocket-recognition capability of a contrastive learning–based model and delineate its practical utility and limitations in SBDD.

 doi:10.20944/preprints202604.0204.v1

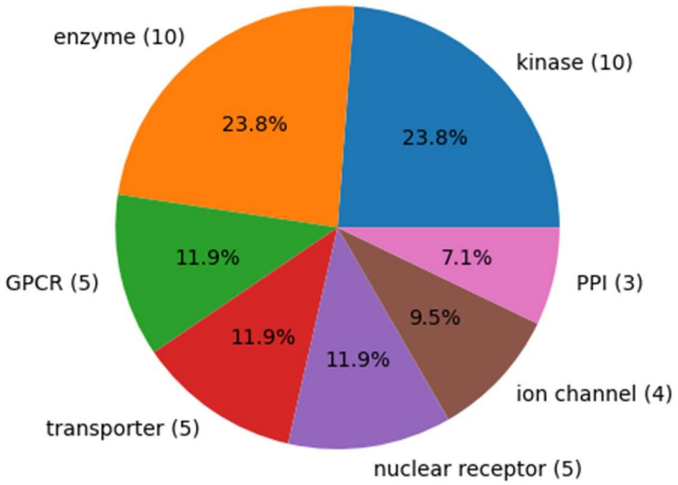

Figure 1. Target classification of benchmarking set. Number of the 42 targets that belong to seven broad protein categories.

2. Materials and Methods

2.1. Benchmark Dataset of 42 Pharmacologically Diverse Targets

A benchmark dataset comprising 42 human protein targets was collected from experimentally determined drug-bound structures deposited in the Protein Data Bank (PDB) [29]. Targets were selected according to three criteria: first, the availability of a pharmacologically relevant small-molecule drug or tool compounds; second, the availability of an experimentally resolved ligand-bound structure suitable for defining the reference binding pocket; and third, the inclusion of therapeutically important targets spanning multiple protein families.

The final benchmark covers seven major classes of drug targets: kinases (n=10), enzymes (n=10), G protein-coupled receptors (GPCRs; n=5), nuclear receptors (n=5), transporters (n=5), ion channels (n=4), and protein-protein interaction (PPI) targets (n=3). As summarized in Table 1, the selected targets span a broad range of therapeutic areas, including oncology, metabolic and endocrine disorders, neurological and psychiatric diseases, inflammatory and autoimmune conditions, cardiovascular disease, infectious disease and rare genetic disorders. The set includes targets modulated by approved drugs or well-characterized tool compounds, thereby providing a pharmacologically relevant and structurally diverse benchmark. For each target, one representative ligand-bound structure was selected as the reference for pocket recognition evaluation.

2.2. Contrastive Learning–Based Model

DrugCLIP is a contrastive learning framework for virtual screening that reformulates protein–ligand matching as a vector-similarity retrieval task [22]. In this approach, protein pockets and small molecules are encoded into a shared latent representation space, and candidate ligands are prioritized according to the similarity of their embeddings. The model employs separate encoders to project protein pockets and small molecules, enabling compatibility between protein–ligand pairs to be inferred directly from embedding proximity. In the original implementation, both encoders are based on the Uni-Mol architecture [30]. The pocket encoder is first pretrained using large-scale synthetic pseudo pocket–ligand pairs generated by the ProFSA strategy [31] and is subsequently fine-tuned together with the molecular encoder using experimentally determined protein–ligand complex structures. During inference, ligands are ranked according to the cosine similarity between molecular and pocket embeddings, enabling rapid virtual screening without explicit docking of every protein–ligand pair.

 doi:10.20944/preprints202604.0204.v1

In this study, DrugCLIP-predicted pocket clusters and associated ligand hits were obtained from the publicly available DrugCLIP database (https://drug-the-whole-genome.yanyanlan.com) [22]. For each target, candidate binding sites were defined according to the pocket clusters reported by DrugCLIP, and pocket recognition performance was evaluated relative to the experimentally validated ligand binding site in the corresponding reference crystal or cryo-EM structure. A prediction was considered successful if at least one retrieved ligand was located within 4 Å of the reference ligand, measured as the distance between the centroids of the two ligands; otherwise, the target was classified as a failed case. All analyses were conducted using the publicly available pretrained DrugCLIP framework and its reported outputs.

2.3. Traditional Pocket Detection Workflow Using Fpocket and ESSA

As a structure-based baseline, candidate ligand-binding pockets were identified using Fpocket [9], a geometric pocket detection method based on Voronoi tessellation and α-sphere representation of protein surfaces. In this framework, surface cavities are described as clusters of spheres with intermediate radii, allowing putative binding sites to be characterized using geometric and physicochemical descriptors. For each protein structure, Fpocket was applied with its default settings to enumerate putative pockets across the entire protein surface.

To incorporate information on protein dynamics, pockets identified by Fpocket were further evaluated using Essential Site Scanning Analysis (ESSA) [28]. ESSA is an elastic-network-model-based method that estimates the functional importance of individual residues by quantifying how local perturbation near each residue alters the low-frequency global modes of the protein. Because these collective modes are closely associated with biologically relevant conformational changes, residues with high ESSA scores are inferred to represent sites whose perturbation is most likely to modulate protein dynamics and, potentially, ligand binding or allosteric regulation.

Following the protocol described in the original ESSA paper [28], a pocket-level ESSA score was defined as either the median or the maximum of the ESSA z-scores of the residues lining that pocket, and the candidate pockets were rank-ordered accordingly. Because ligand binding pockets often exhibit relatively high local hydrophobic density (LHD), this descriptor, as provided by Fpocket[9], was used as an additional filtering criterion. Specifically, a LHD z-score was calculated for each detected pocket, and only pockets with positive LHD z-scores were retained; when ESSA values were very similar among candidate pockets, LHD values were used to further refine the ranking. A prediction was considered successful if the experimentally validated binding pocket was ranked within the top five predicted pockets.

2.4. Structural Coverage Analysis

To evaluate whether DrugCLIP pocket recognition performance was influenced by the prior availability of structural information, we examined the relationship between prediction success and target-specific structural coverage in the Protein Data Bank (PDB) [29]. For each target, structural coverage was quantified using two metrics calculated prior to construction of the benchmark set: the total number of available PDB entries and the number of ligand-bound structures. Targets were then classified according to whether DrugCLIP correctly identified the experimentally validated binding pocket, and the distributions of these structural coverage metrics were compared between successful and unsuccessful cases. This analysis was conducted to determine whether prediction performance primarily reflects the abundance of pre-existing structural data, rather than intrinsic properties of the binding pocket.

 doi:10.20944/preprints202604.0204.v1

Table 1. Benchmark dataset of 42 pharmacologically diverse human protein targets used for pocket recognition evaluation.

Target	UniProtID	Class	Small molecule drug/tool compound	Disease area	PDB
EGFR	P00533	kinase	Osimertinib	NSCLC	6LUD [32]
BRAF	P15056	kinase	Vemurafenib	Melanoma	4RZV [33]
MEK1	Q02750	kinase	Trametinib	Melanoma	7M0Y [34]
ALK	Q9UM73	kinase	Alectinib	NSCLC	3AOX [35]
BTK	Q06187	kinase	Ibrutinib	Leukemia	5P9J [36]
CDK6	Q00534	kinase	Palbociclib	Breast cancer	5L2I [37]
JAK1	P23458	kinase	Upadacitinib	RA	5KHX [38]
PI3Kα	P42336	kinase	Alpelisib	Breast cancer	4JPS [39]
FGFR2	P11362	kinase	Pemigatinib	Cholangiocarcinoma	7WCL [40]
RET	P07949	kinase	Selpercatinib	Thyroid cancer	7DU8
GLP-1R	P43220	GPCR	PF-06882961	Diabetes / Obesity	6X1A [41]
CCR5	P51681	GPCR	Maraviroc	HIV	4MBS [42]
S1P1	P21453	GPCR	Fingolimod	Multiple sclerosis	7EO2 [43]
A2A	P29274	GPCR	Istradefylline	Parkinson	8RW0 [44]
Dopamine D2	P14416	GPCR	Risperidone	Schizophrenia	6CM4 [45]
SCN9A	Q15858	ion channel	BIIB074	Pain	8I5Y [46]
CaV1.2	Q13936	ion channel	Amlodipine	Hypertension	8WE8 [47]
CFTR	P13569	ion channel	Ivacaftor	Cystic fibrosis	6O2P [48]
TRPV1	Q8NER1	ion channel	AMG517	Pain	8JQR [49]
AR	P10275	nuclear receptor	Enzalutamide	Prostate cancer	3V49 [50]
ER	P03372	nuclear receptor	Tamoxifen	Breast cancer	3ERT [51]
PPARG	P37231	nuclear receptor	Pioglitazone	Diabetes	5Y2O [52]
FXR	Q96RI1	nuclear receptor	Obeticholic acid	Liver disease	3FXV [53]
LXR	Q13133	nuclear receptor	GW3965	Metabolic disease	3IPQ [54]
PARP1	P09874	enzyme	Olaparib	Ovarian cancer	7KK4 [55]
DPP4	P27487	enzyme	Sitagliptin	Diabetes	2P8S [56]
PDE5	O76074	enzyme	Sildenafil	ED	1UDT [57]
IDH1	O75874	enzyme	Ivosidenib	AML	8T7O [58]
DHODH	Q02127	enzyme	Leflunomide	RA	3F1Q [59]
SHP2	Q06124	enzyme	RMC-4630	Cancer	7RCT [60]
HDAC1	Q92769	enzyme	Vorinostat	Lymphoma	4LXZ [61]
EZH2	Q15910	enzyme	Tazemetostat	Sarcoma	5LS6 [62]
LSD1	O60341	enzyme	ORY-1001	Leukemia	6K3E
DNMT1	P26358	enzyme	Azacitidine	AML	3SWR
BCL2	P10415	PPI	Venetoclax	Leukemia	6O0K [63]
KRAS	P01116	PPI	Sotorasib	NSCLC	6OIM [64]

 doi:10.20944/preprints202604.0204.v1

Menin	O00255	PPI	Revumenib	AML	7UJ4 [65]
SGLT2	P31639	transporter	Dapagliflozin	Diabetes	8HEZ [66]
SERT	P31645	transporter	Fluvoxamine	Depression	6AWP [67]
VMAT2	Q05940	transporter	Tetrabenazine	Dyskinesia	8T69 [68]
URAT1	Q96S37	transporter	Lesinurad	Gout	9DKB [69]
VAChT	Q16572	transporter	Vesamicol	Neurobiology	8ZMR[70]

3. Results

3.1. Pocket Recognition Performance of DrugCLIP

We first evaluated the ability of DrugCLIP to correctly prioritize the experimentally validated drug-binding pocket across the 42-target benchmark. Overall, DrugCLIP successfully recognize the reference pocket for 31 of 42 targets, corresponding to an overall success rate of 73.8% (Figure 2). However, performance varies substantially across target classes. DrugCLIP achieved perfect success for kinases (10/10), GPCRs (5/5), and nuclear receptors (5/5), indicating that the model can robustly identify canonical ligand-binding pockets in several well-studied target families. Performance was moderate for enzymes and PPIs, for which 6 of 10 targets and 2 of 3 targets, respectively, were correctly predicted. Notably, DrugCLIP failed to localize the binding site of Sotorasib in KRAS (Figure 3), which resides in a shallow pocket formed between the switch-II region and the α3 helix [64], highlighting limitations in recognizing atypical pockets at PPI interfaces.

By contrast, performance was markedly reduced for membrane proteins. Only 2 of 5 transporters and 1 of 4 ion channels were correctly assigned to the validated drug-binding pocket. In particular, DrugCLIP failed to recover the ligand binding sites for VMAT2 (Tetrabenazine) [68], SGLT2 (Dapagliflozin) [66] and VAChT (Vesamicol) [70] among transporters, and for SCN9A (BIIB074) [46], CFTR (Ivacaftor) [48] and TRPV1 (AMG517) [49] among ion channels (Figure 3). These findings suggest that DrugCLIP performs best for targets with conserved, geometrically well-defined orthosteric cavities, but is less reliable for proteins in which ligand-binding sites are conformationally heterogeneous, partially occluded, or difficult to distinguish from alternative cavities. Thus, accurate ligand retrieval in embedding space does not necessarily translate into uniformly reliable pocket recognition across structurally diverse protein families.

These results demonstrate that DrugCLIP has substantial pocket-recognition capability, but its performance is strongly dependent on target class and pocket characteristics. For well-studied protein families with conserved and geometrically well-defined orthosteric sites, such as kinases, GPCRs and nuclear receptors, the model accurately captures key structural determinants of ligand binding. In contrast, its performance declines for proteins with conformationally heterogeneous or membrane-embedded binding sites. This class-dependent behavior suggests that contrastive embedding models capture recurring pocket geometries effectively, yet remain challenged by binding environments that are dynamic, poorly solvent-exposed or difficult to distinguish from competing cavities. As a result, embedding-based ligand retrieval does not uniformly guarantee accurate localization of pharmacologically relevant binding sites across diverse protein systems.

 doi:10.20944/preprints202604.0204.v1

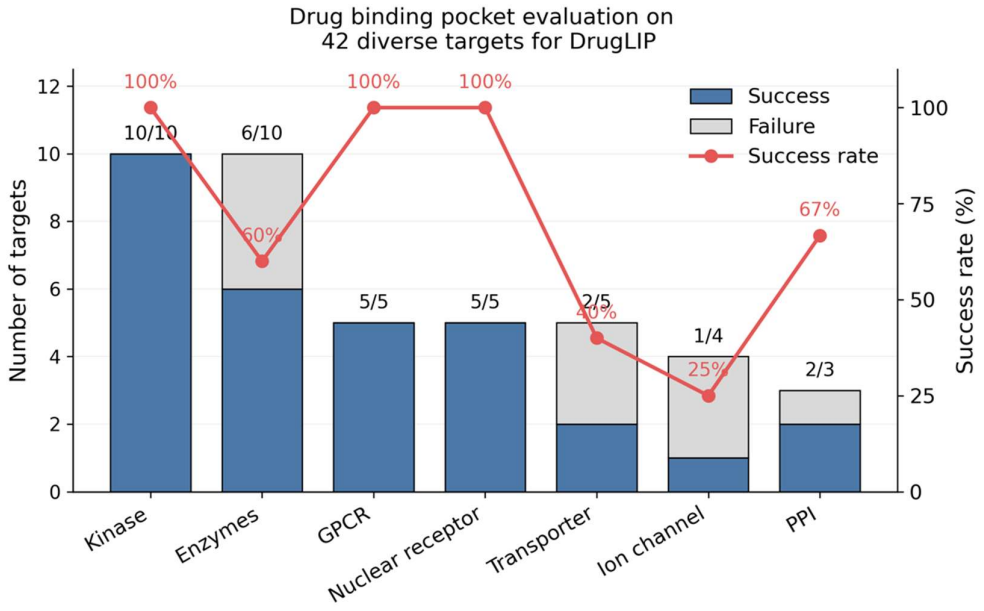

Figure 2. Pocket-recognition performance of DrugCLIP across the 42-target benchmark. DrugCLIP success rates are shown for each major target class. Overall, the model correctly identified the experimentally validated drug-binding pocket for 31 of 42 targets (73.8%). Perfect performance was observed for kinases (10/10), GPCRs (5/5) and nuclear receptors (5/5). Intermediate performance was obtained for enzymes (6/10) and protein–protein interaction (PPI) targets (2/3), whereas substantially lower success rates were observed for transporters (2/5) and ion channels (1/4). Prediction success was defined as recovery of the reference binding pocket among all DrugCLIP pocket clusters.

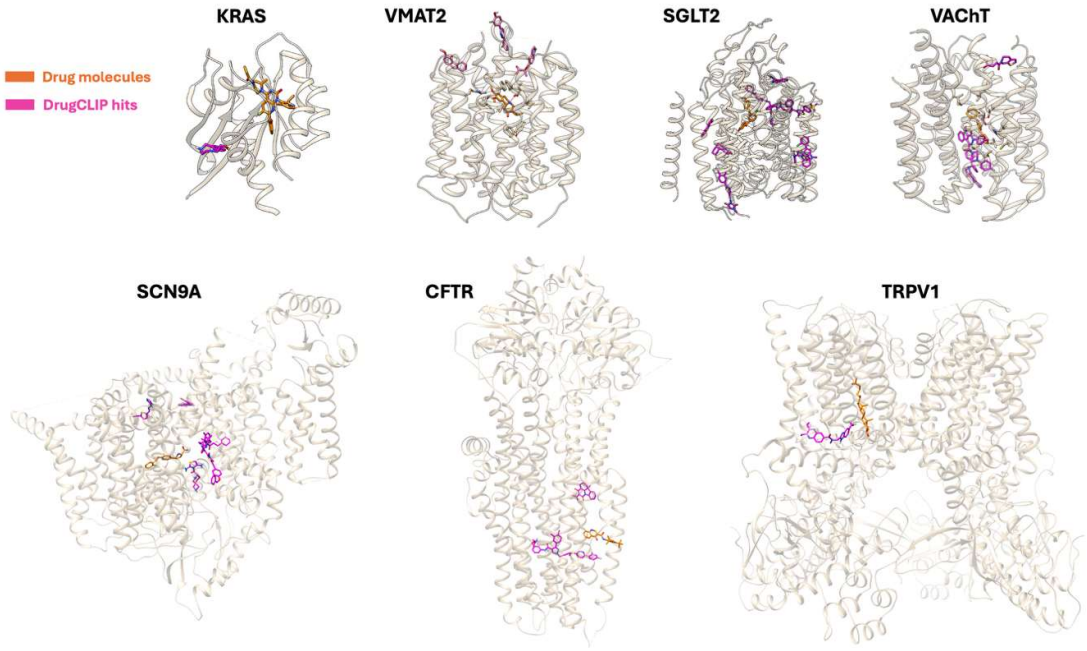

Figure 3. Representative failure cases in DrugCLIP pocket recognition. DrugCLIP failed to correctly localize the experimentally validated drug-binding pocket for several targets. Examples include the binding site of Sotorasib in KRAS (PPI target), transporter binding pockets in VMAT2, SGLT2 and VAChT, and ion-channel binding sites in SCN9A, CFTR and TRPV1. In these systems, the validated ligand-binding sites are often shallow,

 doi:10.20944/preprints202604.0204.v1

conformationally heterogeneous, partially occluded, or embedded within membrane environments, making them difficult to distinguish from alternative surface cavities using embedding-based model.

3.2. Structural Coverage is not Associated with DrugCLIP Pocket-Recognition Success

To assess whether DrugCLIP performance might simply reflect training-data bias, we compared the structural coverage of targets for which DrugCLIP successfully identified the validated binding pocket with that of targets for which it failed (Figure 4). Two complementary measures were considered: the total number of PDB structures available for each target and the number of ligand-bound structures available prior to construction of the benchmark set. In both analyses, the distributions for successful and unsuccessful targets overlapped substantially. Statistical comparison revealed no significant difference in total structural coverage between success and failure cases (P value = 0.35), and no significant difference in ligand-bound structural coverage (P value = 0.19). Therefore, targets that were successfully recognized by DrugCLIP were not simply those with more abundant pre-existing structural information in the PDB.

These results argue against a simple explanation in which DrugCLIP succeeds mainly because closely related structural templates are heavily represented in public databases. Instead, pocket-recognition performance appears to depend more strongly on intrinsic characteristics of the binding itself, such as pocket geometry, accessibility, and how closely the site resembles the pocket patterns captured during model training. Notably, failures were observed even for structurally well-characterized targets, for example, KRAS, for which hundreds of ligand-bound structures (336 entries) are available in the Protein Data Bank, whereas many successful predictions were obtained for targets with only moderate structural coverage. Together, these observations suggest that structural data abundance alone is insufficient to explain DrugCLIP performance.

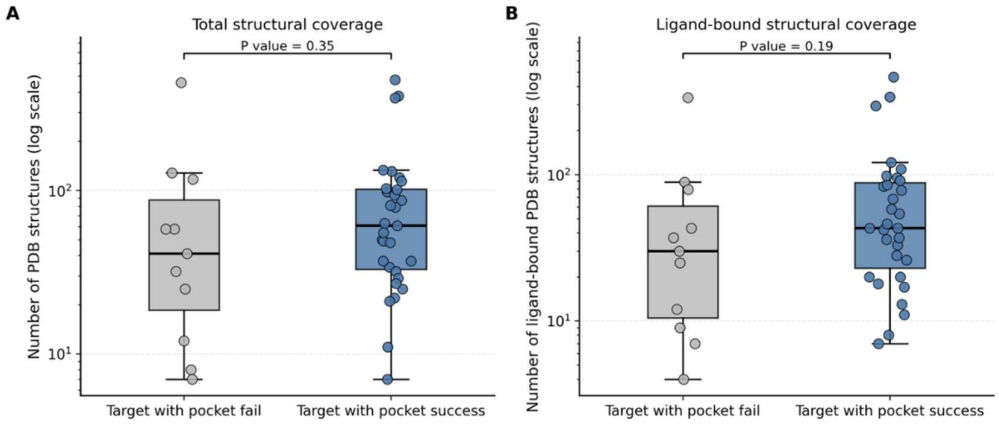

Figure 4. Relationship between DrugCLIP pocket-recognition success and structural coverage. Distribution of structural coverage metrics for targets successfully or unsuccessfully recognized by DrugCLIP. Structural coverage was quantified using (i) the total number of available Protein Data Bank (PDB) structures and (ii) the number of ligand-bound entries available prior to construction of the benchmark set. No significant differences were observed between successful and unsuccessful predictions, indicating that DrugCLIP pocket recognition performance is not strongly associated with the abundance of pre-existing structural data.

3.2. Comparison with a Traditional Fpocket+ESSA Workflow

We next compared DrugCLIP with a conventional structure-based workflow in which candidate pockets identified by Fpocket were further ranked using ESSA-derived scores. When the ESSA_score mean-rank strategy was used, the Fpocket+ESSA workflow correctly recovered the experimentally validated pocket for 33 of 42 targets, corresponding to an overall success rate of 78.6% (Figure 5), which is slightly better than DrugCLIP. Class-specific analysis showed perfect success for kinases

 doi:10.20944/preprints202604.0204.v1

(10/10), GPCRs (5/5), nuclear receptors (5/5), transporters (5/5), and PPI targets (3/3). Performance for enzymes was intermediate (5/10), whereas the method failed completely on ion channels (0/4).

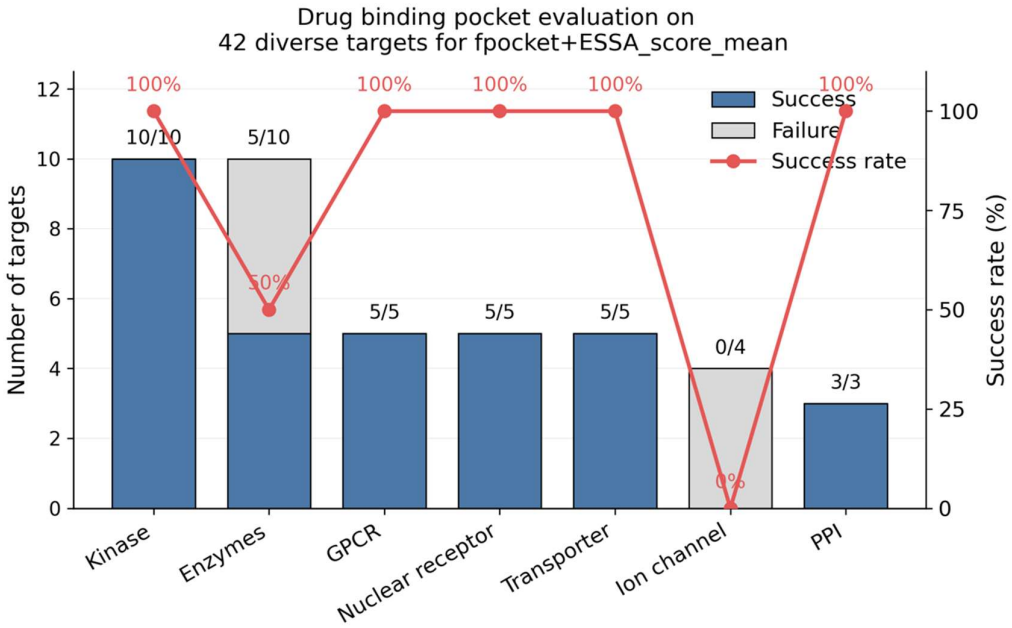

Figure 5. Pocket-recognition performance of the Fpocket+ESSA workflow using the mean-rank scoring scheme. Pocket-recognition success rates across the 42-target benchmark for the traditional structure-based workflow combining Fpocket pocket detection with ESSA-based ranking using the mean ESSA *z*-score aggregation strategy. The workflow correctly identified the experimentally validated binding pocket for 33 of 42 targets (78.6%). Perfect success was observed for kinases, GPCRs, nuclear receptors, transporters and PPIs, whereas performance remained limited for ion channels. Prediction success was defined as recovery of the validated binding pocket within the top 5 ranked candidate pockets.

Using the ESSA_score max-rank strategy, the overall success rate remained 78.6% (33/42), but the class-level distribution shifted slightly (Figure 6). The max-rank scheme preserved perfect performance for kinases (10/10), GPCRs (5/5), nuclear receptors (5/5), transporters (5/5), and PPI targets (3/3), improved ion-channel performance (1/4), but reduced success for enzymes (4/10). Thus, the two ESSA aggregation schemes yielded the same overall accuracy, while redistributing performance across difficult target classes.

 doi:10.20944/preprints202604.0204.v1

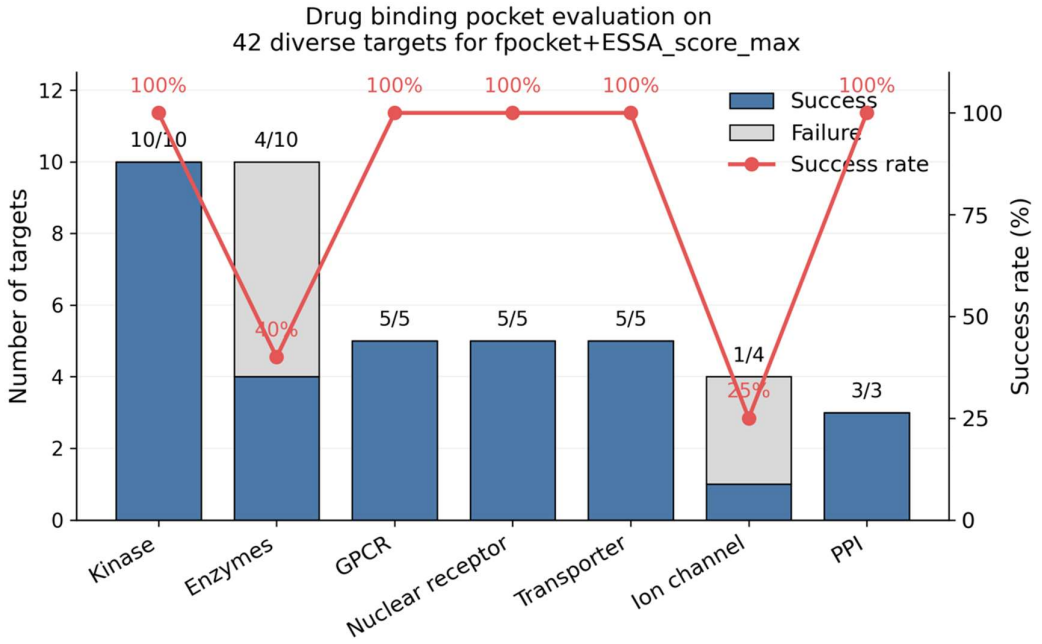

Figure 6. Pocket-recognition performance of the Fpocket+ESSA workflow using the max-rank scoring scheme. Pocket-recognition success rates across the 42-target benchmark for the traditional structure-based workflow combining Fpocket pocket detection with ESSA-based ranking using the maximum ESSA *z*-score scoring scheme. The workflow correctly recovered the experimentally validated binding pocket for 33 of 42 targets (78.6%), matching the overall accuracy obtained with the mean-rank strategy. Perfect success was maintained for kinases, GPCRs, nuclear receptors, transporters and PPIs, whereas performance improved modestly for ion channels but decreased for enzymes. Prediction success was defined as recovery of the validated binding pocket within the top 5 ranked candidate pockets.

Compared with the traditional baseline, DrugCLIP showed a mixed pattern of strengths and limitations. DrugCLIP matched baseline performance for kinases, GPCRs, and nuclear receptors, and slightly outperformed both ESSA variants for other enzymes (6/10 vs. 5/10 and 4/10). However, the traditional Fpocket+ESSA workflow outperformed DrugCLIP for transporters (5/5 vs. 2/5) and PPI targets (3/3 vs. 2/3). For ion channels, all methods performed poorly, although DrugCLIP and the ESSA max-rank strategy each recovered 1 of 4 cases. Overall, these comparisons show that DrugCLIP is competitive with traditional pocket-detection workflows but does not consistently outperform them. Embedding-based representations appear effective for several canonical target families, yet geometry- and dynamics-based pocket analysis remains advantageous for certain challenging systems, particularly transporters. These results emphasize that learned pocket embeddings and traditional structure-based descriptors should be viewed as complementary rather than mutually exclusive strategies for binding site detection.

3.2. ESSA_Score Mean Rank and ESSA_Score Max Rank Performances Are Well Correlated

Although the ESSA_score mean-rank and ESSA_score max-rank strategies produced modestly different outcomes for specific target classes, their pocket rankings were overall well correlated across the benchmark (Figure 7). Most targets clustered in the lower-left region of the plot, indicating that pockets assigned a favorable rank by the mean-based score were generally also assigned a favorable rank by the max-based score. This agreement is especially evident for the successfully recognized cases, where both ranking schemes typically placed the validated pocket within the top few positions. In other words, whether ESSA scores are aggregated using a mean-based or max-based criterion, the resulting pocket order is usually comparable for most targets.

 doi:10.20944/preprints202604.0204.v1

At the same time, a smaller number of outliers deviate from the diagonal, particularly among targets with poorer pocket ranks. These cases indicate that max-based scoring can either promote or demote a candidate pocket relative to the mean-based scheme, thereby affecting performance for specific difficult target classes such as ion channels and other enzymes. Thus, the differences between the two ESSA ranking strategies arise mainly in challenging cases, whereas for most targets they provide a closely similar assessment of pocket relevance.

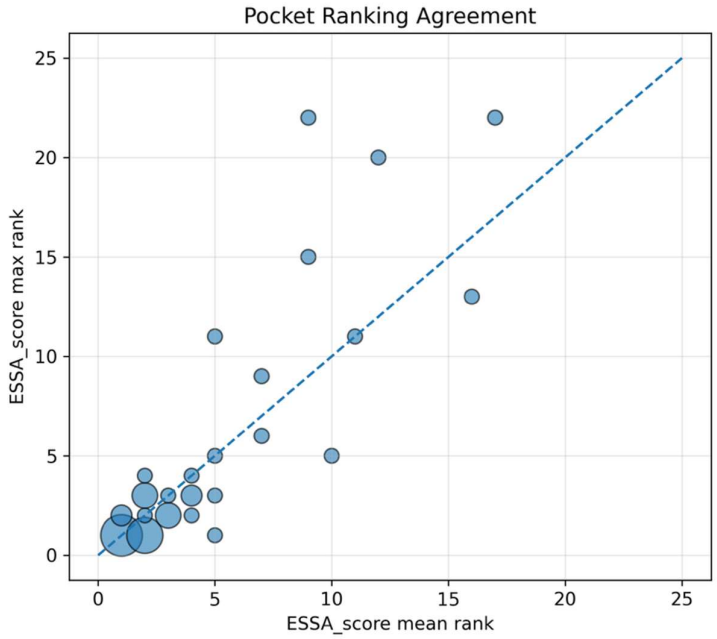

Figure 7. Correlation between ESSA mean-rank and max-rank pocket-ranking strategies. Bubble plot showing the relationship between pocket-ranking positions obtained using ESSA mean-rank and max-rank aggregation schemes across the benchmark dataset. Each bubble represents one or more targets sharing the same ranking positions for the experimentally validated binding pocket, with bubble size proportional to the number of targets. Most bubbles cluster near the lower-rank region and along the diagonal, indicating strong agreement between the two ranking strategies in prioritizing biologically relevant binding sites. Deviations from the diagonal are observed primarily for structurally challenging target.

We next examined how the pocket-recognition success rate changes as a function of the number of top-ranked pockets considered (Figure 8). For both ESSA_score mean-rank and ESSA_score max-rank strategies, the success rate increases steadily as more candidate pockets are included. The two curves are highly similar across the entire range of top N, indicating that the two aggregation schemes yield comparable ranking performance. Both strategies reach ~80% success when the top five pockets are considered, consistent with the benchmark results described above. The max-rank strategy shows slightly higher success for the top one to four pockets.

 doi:10.20944/preprints202604.0204.v1

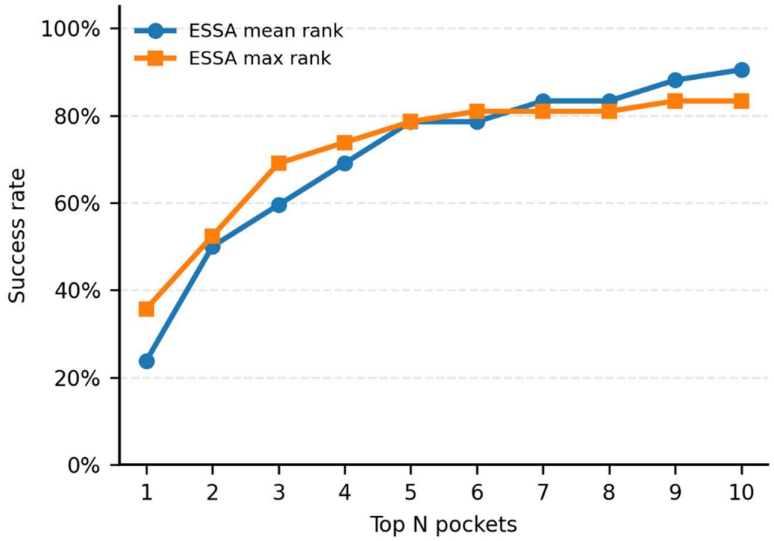

Figure 8. Success rate of pocket recognition as a function of the number of top-ranked pockets considered. Success rates are shown for the Fpocket+ESSA workflow using the ESSA_score mean-rank and ESSA_score max-rank strategies across the 42-target benchmark. A prediction was considered successful if the experimentally validated binding pocket appeared within the top N predicted pockets.

4. Discussion

In this study, we performed a systematic evaluation of the pocket-recognition capability of the contrastive learning–based model DrugCLIP across a pharmacologically diverse benchmark of 42 human drug targets. While embedding-based approaches have demonstrated strong performance in ligand retrieval and virtual screening tasks, their ability to correctly localize biologically relevant ligand-binding sites has remained largely unexplored. By directly comparing DrugCLIP predictions with experimentally validated binding pockets and with a traditional structure-based workflow combining geometric pocket detection and dynamics-informed ranking, our results provide a quantitative assessment of the strengths and limitations of this emerging modelling paradigm.

DrugCLIP exhibited substantial pocket-recognition capability, successfully identifying validated binding sites for 73% of the benchmark targets. Performance was highly robust for canonical drug-target families such as kinases, GPCRs, and nuclear receptors, all of which possess conserved binding cavities with well-defined geometric and physicochemical features. These findings suggest that contrastive embedding models are effective at capturing recurring structural motifs associated with ligand binding. Because such pockets are frequently represented in structural databases and share characteristic spatial patterns, they may be particularly amenable to representation learning strategies that rely on identifying statistical regularities across large datasets.

However, performance declined markedly for more structurally dynamic systems, including membrane transporters and ion channels. In these cases, validated ligand-binding sites are often shallow, conformationally heterogeneous, partially occluded, or embedded within dynamic membrane environments. Such features may reduce the distinguishability of functional binding sites from alternative surface cavities when represented in a latent embedding space. Importantly, several failures occurred even for targets with abundant structural coverage, such as KRAS, indicating that limitations in pocket recognition are not simply attributable to insufficient training data. Instead, intrinsic properties of the binding environment, such as pocket accessibility, flexibility, and the degree of geometric conservation, appear to play a dominant role in determining prediction success.

Comparison with the traditional Fpocket+ESSA workflow further highlights the complementary strengths of embedding-based and structure-based approaches. Although DrugCLIP achieved comparable overall accuracy, the geometry- and dynamics-driven baseline demonstrated superior

 doi:10.20944/preprints202604.0204.v1

performance for transporters and PPIs. These results suggest that methods explicitly incorporating physical descriptors of protein structure and collective dynamics remain advantageous for identifying ligandable sites in challenging systems. Conversely, DrugCLIP showed competitive or improved performance for enzymes, indicating that learned representations can capture aspects of pocket compatibility not fully reflected by geometric criteria alone. Together, these observations argue against viewing embedding-based models as replacements for conventional pocket-detection tools; rather, they support an integrated strategy in which machine learning and physics-based descriptors are combined to improve binding-site identification.

Several limitations of the present study should also be considered. First, the benchmark dataset, while pharmacologically diverse, remains modest in size and is restricted to human targets with available drug-bound structures. Second, pocket recognition was evaluated using a binary success criterion, which does not capture subtler differences in pocket ranking quality. Third, DrugCLIP predictions were assessed using publicly available pretrained models, and further improvements may be achievable through task-specific fine-tuning or incorporation of dynamic structural information. Future work could extend this evaluation to larger and more diverse protein datasets, explore hybrid modelling strategies that integrate embedding similarity with explicit pocket descriptors, and investigate how pocket-recognition accuracy influences prospective virtual screening outcomes.

5. Conclusion

In summary, this study provides a systematic benchmark of binding-site recognition by a contrastive learning–based virtual screening model across a diverse set of clinically relevant drug targets. DrugCLIP demonstrates strong performance for targets with conserved and geometrically well-defined ligand-binding cavities, but its accuracy decreases for proteins with dynamic, shallow, or membrane-embedded binding environments. Importantly, prediction success is not strongly associated with the abundance of pre-existing structural data, suggesting that intrinsic pocket characteristics rather than dataset bias primarily determine performance.

Comparison with a traditional geometry- and dynamics-based pocket-detection workflow (Fpocket+ESSA) reveals that embedding-based approaches are competitive but do not consistently outperform traditional structure-based methods. Instead, the two strategies exhibit complementary strengths across different protein classes. These findings highlight the need for careful validation of binding-site localization when applying embedding-based models in prospective structure-based drug discovery. More broadly, our results suggest that future advances in pocket recognition may benefit from hybrid frameworks that combine learned protein–ligand representations with explicit structural and dynamic descriptors of protein function.

Author Contributions: Conceptualization, C.Y.; methodology, C.Y., B.Y. and P.X.; evaluation, B.Y.; resources, C.Y. and X.G.; writing, C.Y. and B.Y.; visualization, B.Y.; supervision, C.Y. and P.X.; funding acquisition, C.Y. and X.G. All authors have read and agreed to the published version of the manuscript.

Funding: We gratefully acknowledge the financial support by The Fundamental Research Fund of Henan Academy of Sciences (Project NO. 20250626005).

Institutional Review Board Statement: Not applicable.

Data Availability Statement: The datasets analyzed in this study are publicly available. Protein structures were obtained from the Protein Data Bank (PDB). DrugCLIP predictions were obtained from the publicly available DrugCLIP database (https://drug-the-whole-genome.yanyanlan.com). The benchmark dataset used in this study is provided in Table 1 of the manuscript.

Acknowledgments: During the preparation of this manuscript, the authors used ChatGPT for the purposes of improving the readability and language of the manuscript. The authors have reviewed and edited the output and take full responsibility for the content of this publication.

Conflicts of Interest: All authors declare no competing interests.

 doi:10.20944/preprints202604.0204.v1

Abbreviations

The following abbreviations are used in this manuscript:

SBDD	structure-based drug discovery
ESSA	essential site scanning analysis
PPI	protein-protein interactions
LHD	local hydrophobic density
PDB	Protein Data Bank
GPCR	G protein-coupled receptor

References

1. Bohacek, R.S.; McMartin, C.; Guida, W.C. The art and practice of structure-based drug design: a molecular modeling perspective. *Med. Res. Rev.* **1996**, *16*, 3-50.
2. Sadybekov, A.V.; Katritch, V. Computational approaches streamlining drug discovery. *Nature* **2023**, *616*, 673-685.
3. Lionta, E.; Spyrou, G.; K Vassilatis, D.; Cournia, Z. Structure-based virtual screening for drug discovery: principles, applications and recent advances. *Curr. Top. Med. Chem.* **2014**, *14*, 1923-1938.
4. Talele, T.T.; Khedkar, S.A.; Rigby, A.C. Successful applications of computer aided drug discovery: moving drugs from concept to the clinic. *Curr. Top. Med. Chem.* **2010**, *10*, 127-141.
5. Yang, C.; Chen, E.A.; Zhang, Y. Protein–ligand docking in the machine-learning era. *Molecules* **2022**, *27*, 4568.
6. Ferreira, L.G.; Dos Santos, R.N.; Oliva, G.; Andricopulo, A.D. Molecular docking and structure-based drug design strategies. *Molecules* **2015**, *20*, 13384-13421.
7. Liu, Y.; Grimm, M.; Dai, W.-t.; Hou, M.-c.; Xiao, Z.-X.; Cao, Y. CB-Dock: a web server for cavity detection-guided protein–ligand blind docking. *Acta Pharmacol. Sin.* **2020**, *41*, 138-144.
8. Zhang, W.; Bell, E.W.; Yin, M.; Zhang, Y. EDock: blind protein–ligand docking by replica-exchange monte carlo simulation. *J. Cheminform.* **2020**, *12*, 37.
9. Schmidtke, P.; Le Guilloux, V.; Maupetit, J.; Tuffery, P. Fpocket: online tools for protein ensemble pocket detection and tracking. *Nucleic Acids Res.* **2010**, *38*, W582-W589.
10. Ngan, C.H.; Bohnuud, T.; Mottarella, S.E.; Beglov, D.; Villar, E.A.; Hall, D.R.; Kozakov, D.; Vajda, S. FTMAP: extended protein mapping with user-selected probe molecules. *Nucleic Acids Res.* **2012**, *40*, W271-W275.
11. Halgren, T.A. Identifying and characterizing binding sites and assessing druggability. *J. Chem. Inf. Model.* **2009**, *49*, 377-389.
12. Schmidtke, P.; Bidon-Chanal, A.; Luque, F.J.; Barril, X. MDpocket: open-source cavity detection and characterization on molecular dynamics trajectories. *Bioinformatics* **2011**, *27*, 3276-3285.
13. Rooklin, D.; Wang, C.; Katigbak, J.; Arora, P.S.; Zhang, Y. AlphaSpace: fragment-centric topographical mapping to target protein–protein interaction interfaces. *J. Chem. Inf. Model.* **2015**, *55*, 1585-1599.
14. Katigbak, J.; Li, H.; Rooklin, D.; Zhang, Y. AlphaSpace 2.0: representing concave biomolecular surfaces using β-clusters. *J. Chem. Inf. Model.* **2020**, *60*, 1494-1508.
15. Cramer, P. AlphaFold2 and the future of structural biology. *Nat. Struct. Mol. Biol.* **2021**, *28*, 704-705.
16. Jumper, J.; Evans, R.; Pritzel, A.; Green, T.; Figurnov, M.; Ronneberger, O.; Tunyasuvunakool, K.; Bates, R.; Žídek, A.; Potapenko, A. Highly accurate protein structure prediction with AlphaFold. *Nature* **2021**, *596*, 583-589.
17. Baek, M.; DiMaio, F.; Anishchenko, I.; Dauparas, J.; Ovchinnikov, S.; Lee, G.R.; Wang, J.; Cong, Q.; Kinch, L.N.; Schaeffer, R.D. Accurate prediction of protein structures and interactions using a three-track neural network. *Science* **2021**, *373*, 871-876.
18. Abramson, J.; Adler, J.; Dunger, J.; Evans, R.; Green, T.; Pritzel, A.; Ronneberger, O.; Willmore, L.; Ballard, A.J.; Bambrick, J. Accurate structure prediction of biomolecular interactions with AlphaFold 3. *Nature* **2024**, *630*, 493-500.
19. Passaro, S.; Corso, G.; Wohlwend, J.; Reveiz, M.; Thaler, S.; Somnath, V.R.; Getz, N.; Portnoi, T.; Roy, J.; Stark, H. Boltz-2: Towards accurate and efficient binding affinity prediction. *BioRxiv* **2025**.

 doi:10.20944/preprints202604.0204.v1

20. Team, P.; Zhang, Y.; Gong, C.; Zhang, H.; Ma, W.; Liu, Z.; Chen, X.; Guan, J.; Wang, L.; Yang, Y. Protenix-v1: Toward high-accuracy open-source biomolecular structure prediction. *BioRxiv* **2026**, 2026.2002. 2005.703733.
21. Corso, G.; Stärk, H.; Jing, B.; Barzilay, R.; Jaakkola, T. Diffdock: Diffusion steps, twists, and turns for molecular docking. *arXiv preprint arXiv:2210.01776* **2022**.
22. Jia, Y.; Gao, B.; Tan, J.; Zheng, J.; Hong, X.; Zhu, W.; Tan, H.; Xiao, Y.; Tan, L.; Cai, H. Deep contrastive learning enables genome-wide virtual screening. *Science* **2026**, *391*, eads9530.
23. Luo, D.; Liu, D.; Qu, X.; Dong, L.; Wang, B. Enhancing generalizability in protein–ligand binding affinity prediction with multimodal contrastive learning. *J. Chem. Inf. Model.* **2024**, *64*, 1892-1906.
24. Singh, R.; Sledzieski, S.; Bryson, B.; Cowen, L.; Berger, B. Contrastive learning in protein language space predicts interactions between drugs and protein targets. *Proc. Natl. Acad. Sci. U.S.A.* **2023**, *120*, e2220778120.
25. Škrinjar, P.; Eberhardt, J.; Durairaj, J.; Schwede, T. Have protein-ligand co-folding methods moved beyond memorisation? *BioRxiv* **2025**, 2025.2002. 2003.636309.
26. Wei, H.; McCammon, J.A. Structure and dynamics in drug discovery. *npj Drug Discov.* **2024**, *1*, 1.
27. Tran-Nguyen, V.-K.; Jacquemard, C.; Rognan, D. LIT-PCBA: an unbiased data set for machine learning and virtual screening. *J. Chem. Inf. Model.* **2020**, *60*, 4263-4273.
28. Kaynak, B.T.; Bahar, I.; Doruker, P. Essential site scanning analysis: A new approach for detecting sites that modulate the dispersion of protein global motions. *Comput. Struct. Biotechnol. J.* **2020**, *18*, 1577-1586.
29. Liu, Z.; Li, Y.; Han, L.; Li, J.; Liu, J.; Zhao, Z.; Nie, W.; Liu, Y.; Wang, R. PDB-wide collection of binding data: current status of the PDBbind database. *Bioinformatics* **2015**, *31*, 405-412.
30. Zhou, G.; Gao, Z.; Ding, Q.; Zheng, H.; Xu, H.; Wei, Z.; Zhang, L.; Ke, G. Uni-mol: A universal 3d molecular representation learning framework. In Proceedings of the The eleventh international conference on learning representations, 2023.
31. Gao, B.; Jia, Y.; Mo, Y.; Ni, Y.; Ma, W.; Ma, Z.; Lan, Y. Profsa: Self-supervised pocket pretraining via protein fragment-surroundings alignment. *arXiv preprint arXiv:2310.07229* **2023**.
32. Kashima, K.; Kawauchi, H.; Tanimura, H.; Tachibana, Y.; Chiba, T.; Torizawa, T.; Sakamoto, H. CH7233163 overcomes osimertinib-resistant EGFR-Del19/T790M/C797S mutation. *Mol. Cancer Ther.* **2020**, *19*, 2288-2297.
33. Karoulia, Z.; Wu, Y.; Ahmed, T.A.; Xin, Q.; Bollard, J.; Krepler, C.; Wu, X.; Zhang, C.; Bollag, G.; Herlyn, M. An integrated model of RAF inhibitor action predicts inhibitor activity against oncogenic BRAF signaling. *Cancer Cell* **2016**, *30*, 485-498.
34. Gonzalez-Del Pino, G.L.; Li, K.; Park, E.; Schmoker, A.M.; Ha, B.H.; Eck, M.J. Allosteric MEK inhibitors act on BRAF/MEK complexes to block MEK activation. *Proc. Natl. Acad. Sci. U.S.A.* **2021**, *118*, e2107207118.
35. Sakamoto, H.; Tsukaguchi, T.; Hiroshima, S.; Kodama, T.; Kobayashi, T.; Fukami, T.A.; Oikawa, N.; Tsukuda, T.; Ishii, N.; Aoki, Y. CH5424802, a selective ALK inhibitor capable of blocking the resistant gatekeeper mutant. *Cancer Cell* **2011**, *19*, 679-690.
36. Bender, A.T.; Gardberg, A.; Pereira, A.; Johnson, T.; Wu, Y.; Grenningloh, R.; Head, J.; Morandi, F.; Haselmayer, P.; Liu-Bujalski, L. Ability of Bruton's tyrosine kinase inhibitors to sequester Y551 and prevent phosphorylation determines potency for inhibition of Fc receptor but not B-cell receptor signaling. *Mol. Pharmacol.* **2017**, *91*, 208-219.
37. Chen, P.; Lee, N.V.; Hu, W.; Xu, M.; Ferre, R.A.; Lam, H.; Bergqvist, S.; Solowiej, J.; Diehl, W.; He, Y.-A. Spectrum and degree of CDK drug interactions predicts clinical performance. *Mol. Cancer Ther.* **2016**, *15*, 2273-2281.
38. Caspers, N.L.; Han, S.; Rajamohan, F.; Hoth, L.R.; Geoghegan, K.F.; Subashi, T.A.; Vazquez, M.L.; Kaila, N.; Cronin, C.N.; Johnson, E. Development of a high-throughput crystal structure-determination platform for JAK1 using a novel metal-chelator soaking system. *Acta Crystallogr. F* **2016**, *72*, 840-845.
39. Furet, P.; Guagnano, V.; Fairhurst, R.A.; Imbach-Weese, P.; Bruce, I.; Knapp, M.; Fritsch, C.; Blasco, F.; Blanz, J.; Aichholz, R. Discovery of NVP-BYL719 a potent and selective phosphatidylinositol-3 kinase alpha inhibitor selected for clinical evaluation. *Bioorg. Med. Chem. Lett.* **2013**, *23*, 3741-3748.
40. Lin, Q.; Chen, X.; Qu, L.; Guo, M.; Wei, H.; Dai, S.; Jiang, L.; Chen, Y. Characterization of the cholangiocarcinoma drug pemigatinib against FGFR gatekeeper mutants. *Commun. Chem.* **2022**, *5*, 100.

 doi:10.20944/preprints202604.0204.v1

41. Zhang, X.; Belousoff, M.J.; Zhao, P.; Kooistra, A.J.; Truong, T.T.; Ang, S.Y.; Underwood, C.R.; Egebjerg, T.; Šenel, P.; Stewart, G.D. Differential GLP-1R binding and activation by peptide and non-peptide agonists. *Mol. Cell* **2020**, *80*, 485-500. e487.
42. Tan, Q.; Zhu, Y.; Li, J.; Chen, Z.; Han, G.W.; Kufareva, I.; Li, T.; Ma, L.; Fenalti, G.; Li, J. Structure of the CCR5 chemokine receptor–HIV entry inhibitor maraviroc complex. *Science* **2013**, *341*, 1387-1390.
43. Xu, Z.; Ikuta, T.; Kawakami, K.; Kise, R.; Qian, Y.; Xia, R.; Sun, M.-X.; Zhang, A.; Guo, C.; Cai, X.-H. Structural basis of sphingosine-1-phosphate receptor 1 activation and biased agonism. *Nat. Chem. Biol.* **2022**, *18*, 281-288.
44. Glover, H.; Saßmannshausen, T.; Bertrand, Q.; Trabuco, M.; Slavov, C.; Bacchin, A.; Andres, F.; Kondo, Y.; Stipp, R.; Wranik, M. Photoswitch dissociation from a G protein-coupled receptor resolved by time-resolved serial crystallography. *Nat. Commun.* **2024**, *15*, 10837.
45. Wang, S.; Che, T.; Levit, A.; Shoichet, B.K.; Wacker, D.; Roth, B.L. Structure of the D2 dopamine receptor bound to the atypical antipsychotic drug risperidone. *Nature* **2018**, *555*, 269-273.
46. Wu, Q.; Huang, J.; Fan, X.; Wang, K.; Jin, X.; Huang, G.; Li, J.; Pan, X.; Yan, N. Structural mapping of Nav1. 7 antagonists. *Nat. Commun.* **2023**, *14*, 3224.
47. Gao, S.; Yao, X.; Chen, J.; Huang, G.; Fan, X.; Xue, L.; Li, Z.; Wu, T.; Zheng, Y.; Huang, J. Structural basis for human Cav1. 2 inhibition by multiple drugs and the neurotoxin calciseptine. *Cell* **2023**, *186*, 5363-5374. e5316.
48. Liu, F.; Zhang, Z.; Levit, A.; Levring, J.; Touhara, K.K.; Shoichet, B.K.; Chen, J. Structural identification of a hotspot on CFTR for potentiation. *Science* **2019**, *364*, 1184-1188.
49. Fan, J.; Ke, H.; Lei, J.; Wang, J.; Tominaga, M.; Lei, X. Structural basis of TRPV1 inhibition by SAF312 and cholesterol. *Nat. Commun.* **2024**, *15*, 6689.
50. Nique, F.; Hebbe, S.; Peixoto, C.; Annoot, D.; Lefrançois, J.-M.; Duval, E.; Michoux, L.; Triballeau, N.; Lemoullec, J.-M.; Mollat, P. Discovery of diarylhydantoins as new selective androgen receptor modulators. *J. Med. Chem.* **2012**, *55*, 8225-8235.
51. Shiau, A.K.; Barstad, D.; Loria, P.M.; Cheng, L.; Kushner, P.J.; Agard, D.A.; Greene, G.L. The structural basis of estrogen receptor/coactivator recognition and the antagonism of this interaction by tamoxifen. *Cell* **1998**, *95*, 927-937.
52. Lee, M.A.; Tan, L.; Yang, H.; Im, Y.-G.; Im, Y.J. Structures of PPARγ complexed with lobeglitazone and pioglitazone reveal key determinants for the recognition of antidiabetic drugs. *Sci. Rep.* **2017**, *7*, 16837.
53. Feng, S.; Yang, M.; Zhang, Z.; Wang, Z.; Hong, D.; Richter, H.; Benson, G.M.; Bleicher, K.; Grether, U.; Martin, R.E. Identification of an N-oxide pyridine GW4064 analog as a potent FXR agonist. *Bioorg. Med. Chem. Lett.* **2009**, *19*, 2595-2598.
54. Fradera, X.; Vu, D.; Nimz, O.; Skene, R.; Hosfield, D.; Wynands, R.; Cooke, A.J.; Haunsø, A.; King, A.; Bennett, D.J. X-ray structures of the LXRα LBD in its homodimeric form and implications for heterodimer signaling. *J. Mol. Biol.* **2010**, *399*, 120-132.
55. Ryan, K.; Bolaňos, B.; Smith, M.; Palde, P.B.; Cuenca, P.D.; VanArsdale, T.L.; Niessen, S.; Zhang, L.; Behenna, D.; Ornelas, M.A. Dissecting the molecular determinants of clinical PARP1 inhibitor selectivity for tankyrase1. *J. Biol. Chem.* **2021**, *296*.
56. Biftu, T.; Scapin, G.; Singh, S.; Feng, D.; Becker, J.W.; Eiermann, G.; He, H.; Lyons, K.; Patel, S.; Petrov, A. Rational design of a novel, potent, and orally bioavailable cyclohexylamine DPP-4 inhibitor by application of molecular modeling and X-ray crystallography of sitagliptin. *Bioorg. Med. Chem. Lett.* **2007**, *17*, 3384-3387.
57. Sung, B.-J.; Yeon Hwang, K.; Ho Jeon, Y.; Lee, J.I.; Heo, Y.-S.; Hwan Kim, J.; Moon, J.; Min Yoon, J.; Hyun, Y.-L.; Kim, E. Structure of the catalytic domain of human phosphodiesterase 5 with bound drug molecules. *Nature* **2003**, *425*, 98-102.
58. McCoy, M.A.; Lu, J.; Richard Miller, F.; Soisson, S.M.; Lam, M.H.; Fischer, C. Biostructural, biochemical and biophysical studies of mutant IDH1. *Nat. Commun.* **2024**, *15*, 7877.
59. Davies, M.; Heikkila, T.; McConkey, G.A.; Fishwick, C.W.; Parsons, M.R.; Johnson, A.P. Structure-based design, synthesis, and characterization of inhibitors of human and Plasmodium falciparum dihydroorotate dehydrogenases. *J. Med. Chem.* **2009**, *52*, 2683-2693.

 doi:10.20944/preprints202604.0204.v1

60. Vemulapalli, V.; Donovan, K.A.; Seegar, T.C.; Rogers, J.M.; Bae, M.; Lumpkin, R.J.; Cao, R.; Henke, M.T.; Ray, S.S.; Fischer, E.S. Targeted degradation of the oncogenic phosphatase SHP2. *Biochemistry* **2021**, *60*, 2593-2609.
61. Lauffer, B.E.; Mintzer, R.; Fong, R.; Mukund, S.; Tam, C.; Zilberleyb, I.; Flicke, B.; Ritscher, A.; Fedorowicz, G.; Vallero, R. Histone deacetylase (HDAC) inhibitor kinetic rate constants correlate with cellular histone acetylation but not transcription and cell viability. *J. Biol. Chem.* **2013**, *288*, 26926-26943.
62. Vaswani, R.G.; Gehling, V.S.; Dakin, L.A.; Cook, A.S.; Nasveschuk, C.G.; Duplessis, M.; Iyer, P.; Balasubramanian, S.; Zhao, F.; Good, A.C. Identification of (R)-N-((4-Methoxy-6-methyl-2-oxo-1, 2-dihydropyridin-3-yl) methyl)-2-methyl-1-(1-(1-(2, 2, 2-trifluoroethyl) piperidin-4-yl) ethyl)-1 H-indole-3-carboxamide (CPI-1205), a Potent and Selective Inhibitor of Histone Methyltransferase EZH2, Suitable for Phase I Clinical Trials for B-Cell Lymphomas. *J. Med. Chem.* **2016**, *59*, 9928-9941.
63. Birkinshaw, R.W.; Gong, J.-n.; Luo, C.S.; Lio, D.; White, C.A.; Anderson, M.A.; Blombery, P.; Lessene, G.; Majewski, I.J.; Thijssen, R. Structures of BCL-2 in complex with venetoclax reveal the molecular basis of resistance mutations. *Nat. Commun.* **2019**, *10*, 2385.
64. Canon, J.; Rex, K.; Saiki, A.Y.; Mohr, C.; Cooke, K.; Bagal, D.; Gaida, K.; Holt, T.; Knutson, C.G.; Koppada, N. The clinical KRAS (G12C) inhibitor AMG 510 drives anti-tumour immunity. *Nature* **2019**, *575*, 217-223.
65. Perner, F.; Stein, E.M.; Wenge, D.V.; Singh, S.; Kim, J.; Apazidis, A.; Rahnamoun, H.; Anand, D.; Marinaccio, C.; Hatton, C. MEN1 mutations mediate clinical resistance to menin inhibition. *Nature* **2023**, *615*, 913-919.
66. Hiraizumi, M.; Akashi, T.; Murasaki, K.; Kishida, H.; Kumanomidou, T.; Torimoto, N.; Nureki, O.; Miyaguchi, I. Transport and inhibition mechanism of the human SGLT2–MAP17 glucose transporter. *Nat. Struct. Mol. Biol.* **2024**, *31*, 159-169.
67. Coleman, J.A.; Gouaux, E. Structural basis for recognition of diverse antidepressants by the human serotonin transporter. *Nat. Struct. Mol. Biol.* **2018**, *25*, 170-175.
68. Pidathala, S.; Liao, S.; Dai, Y.; Li, X.; Long, C.; Chang, C.-L.; Zhang, Z.; Lee, C.-H. Mechanisms of neurotransmitter transport and drug inhibition in human VMAT2. *Nature* **2023**, *623*, 1086-1092.
69. Suo, Y.; Fedor, J.G.; Zhang, H.; Tsolova, K.; Shi, X.; Sharma, K.; Kumari, S.; Borgnia, M.; Zhan, P.; Im, W. Molecular basis of the urate transporter URAT1 inhibition by gout drugs. *Nat. Commun.* **2025**, *16*, 5178.
70. Zhang, Y.; Dai, F.; Chen, N.; Zhou, D.; Lee, C.-H.; Song, C.; Zhang, Y.; Zhang, Z. Structural insights into VAChT neurotransmitter recognition and inhibition. *Cell Res.* **2024**, *34*, 665-668.